IEEE Access
Multidisciplinary | Rapid Review | Open Access Journal

Received March 13, 2021, accepted April 7, 2021, date of publication April 12, 2021, date of current version April 28, 2021.

Digital Object Identifier 10.1109/ACCESS.2021.3072700

Fault Tolerant Sensorless Control Strategy With Multi-States Switching Method for In-Wheel Electric Vehicle

ZIHUI WANG, JINCAI SHAO, AND ZHIYUAN HE
Department of Automation and Electrical Engineering, Zhejiang University of Science and Technology, Hangzhou 310023, China
Corresponding author: Zihui Wang (wzh2718@zust.edu.cn)

This work was supported by the Natural Science Foundation of Zhejiang Province, China under Grant LQ17E070002.

ABSTRACT The in-wheel electric vehicle with distributed drive units has better stability and flexibility than traditional centralized drives, but may encounter a higher failure rate due to additional actuators and sensors, especially that the faults of the wheel-side position sensor make motor torque out of control. To overcome this problem, a fault-tolerant control strategy with a multi-states switching method is proposed. The strategy judges the sensor failure by verifying redundant speed information, realizes sensorless control schemes by flux-observer based algorithm in high-speed range and I-F control algorithm in low-speed range with low acoustic noise, and applies adaptive transition process between different control schemes. To pursuit high stability, the signal-to-noise analysis for fault judgment due to sensorless estimation accuracy is discussed. Meanwhile, the principle of I-F resonant oscillations during the transition process is initially deduced in detail, and the conclusion of stability condition is obtained. Finally, the influence of system parameters on resonance performance is analyzed by simulation, and the effectiveness and reliability of the proposed strategy for the risk-controlling process are verified by experiments.

INDEX TERMS In-wheel permanent magnet synchronous motor, position sensor failure, fault-tolerant control, multi-states switching, I-F resonant oscillations.

I. INTRODUCTION

Electric vehicles with in-wheel motor drive systems have the advantages of compact structure, high transmission efficiency and flexible torque controllability. The redundant drive units can effectively improve the stability of the vehicle but have a higher failure probability due to the large number of actuators and sensors. When single or multiple driving units fail at high running speed, the output torque among all driving wheels is unbalanced, which may lead to the loss of control on longitudinal and lateral directions, threatening the safety and stability of vehicle driving [1].

To maintain good driving performance under partial failure conditions, the Fault-Tolerant Control (FTC) strategies have been widely studied, and several torque distribution control methods are proposed recently. When the fault occurs, these methods take the parameters of yaw rate, additional yaw torque, lateral acceleration, and longitudinal acceleration as inputs, and using direct solving or iterative algorithms for objective functions minimization [2]–[9], to control torque on all healthy wheels and maintain the body attitude of the car. However, if the power of the faulty wheel being cut off immediately at the moment of failure, strong torque ripples may be generated, which influence the dynamic performance of the torque distribution control in a certain period. Therefore, improved FTC strategies are considered to keep the faulty wheel on-line under specific fault conditions, and keep the torque control available to achieve a pseudo-full-wheel control.

The failures of in-wheel drive systems usually involve the in-wheel motor faults [10]–[11], the power inverter faults [12], and the sensor faults [13]–[14]. Considering the sensor faults, the position sensors such as the resolver, hall-sensor, or photoelectric encoder used in vehicles are easily disturbed by mechanical impact, moisture corrosion, and electromagnetic interference, resulting in signal loss or measurement deviation. These faults cause current vector decoupling error and deteriorate the performance of current

The associate editor coordinating the review of this manuscript and approving it for publication was Moussa Boukhnifer.

and torque closed-loop controls. To overcome the problem, [15]–[19] propose several fault-tolerant control methods based on a sensorless algorithm, so that the controller can obtain rotor position and speed information without sensors, and achieve fault-tolerant and safe coasting operations by the fast current response and torque control. In [17], the rotor position information of the in-wheel motor is obtained by the High-Frequency (HF) voltage injection method. The advanced phase injections solve the problem of limited estimation accuracy that be affected by the carrier frequency, and improves the position angle tracking accuracy and dynamic performance in the low-speed range. In [18], an HF injection method with a generalized integrator is used to realize the fast and smooth switching at the moment of sensor failure under low-speed with load conditions. The transient fault process lasts only 40ms and the stable fault-tolerant operation has good anti-interference performance. In [19], a composite sensorless FTC strategy suitable for a wide speed range is proposed, which combines the HF rotating-voltage injection method in low-speed range with the stator flux estimation method in the high-speed range, and considers the details of the transition process in the algorithm switching period. It should be pointed out that the HF-injection-based sensorless algorithm at low speed has a significant disadvantage due to its strong acoustic noise. The injected 0.5k-1kHz signals can produce noisy howling which seriously affects the driving experience so that it is not suitable for vehicle applications. To overcome this drawback, a wide speed range FTC strategy without acoustic noise is proposed in this paper. By using the flux-observer based Field-Oriented Vector (FOC) control in the high-speed range and the self-resonance principle of current frequency (I-F) control in the low-speed range, the reliability of the FTC strategy is improved, and the switching process of multi-state sensorless algorithm is designed to be smooth as well.

The paper introduces the proposed strategy as follows. In Section II the combined sensorless control methods based on redundant position information detection are presented. Meanwhile, the principle of the I-F resonant oscillation process is deducted in detail. The design of the multi-states switching process in a wide speed range is proposed in Section III. The effectiveness of the strategy for a smooth transition and safe deceleration is illustrated in Section IV. Finally, conclusions are made in the last section.

II. MODELING OF SENSORLESS FAULT TOLERANT CONTROL

A. FAILURE LOGIC JUDGMENT OF POSITION SENSOR

The Permanent Magnet Synchronous Motor (PMSM) or Permanent Magnet Brushless Motor (BLDC) is usually adopted in in-wheel drive systems, and the efficient torque controls are realized by closed-loop FOC algorithms. The topology of a single in-wheel drive unit is shown in Fig. 1. The position sensor provides the rotor angle information to the controller, and the controller uses the rotor angle to decouple the stator current vector into the d-axis excitation component and

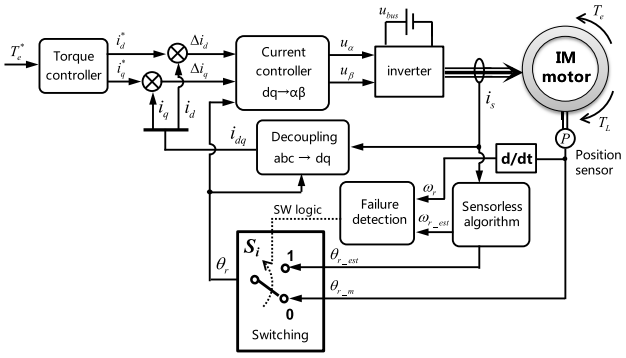

FIGURE 1. The fault-tolerant control structure for the in-wheel motor drive system.

q-axis torque component, so as to control flux and torque independently.

When the position sensor fails, the deviation of the rotor angle will lead to inefficient current control and deterioration of torque characteristics. Therefore, the sensorless estimation algorithm is embedded into the control strategy to verify the sensor signals and make the failure logic judgment. Considering redundancy in the multi-wheel drive system that both the position sensor and sensorless algorithm applied on each wheel can provide speed and position information, then the sensor failure judgment mechanism can be given as:

$$S_k = \begin{cases} 1, \left| \int_T (\omega_{rk} - \varpi) dt \right| > \gamma \text{healthy} \\ 0, \left| \int_T (\omega_{rk} - \varpi) dt \right| \le \gamma \text{faulty} \end{cases} \tag{1}$$

$$\varpi = \frac{1}{2N-1} \left(\sum_{i \in A} \omega_{ri\_est} + \sum_{j \in B} \omega_{rj} \right) \tag{2}$$

where S_k is the failure judgment logic of the k-th drive unit, T is the monitoring cycle, ω_r is the measured speed of the sensor, ω_{r-est} is the estimated speed, ϖ is the weighted average speed, and γ is the error threshold of accumulated angle. Set A contains all the numbers of drive units, set B represents the unit numbers except for the failed ones, and N is the number of drive wheels. For the distributed full-wheel direct drive structure, the number N equals 4 so that the average speed can be obtained from the other 7 speed signals. Once the failure logic of a driving unit is determined to be 1, the number is excluded from sets A and B, and sensor failures of the remaining driving wheels are continuously being monitored.

B. TORQUE CONTROL BASED ON SENSORLESS ALGORITHM

1) MODEL OF IN-WHEEL PMSM

In the permanent magnet in-wheel motor, the torque control is realized by decoupling the stator current into the torque component and the excitation component. The electromagnetic torque can be described in dq coordinate as

$$T_e = \frac{3}{2} P(\psi_d i_q - \psi_q i_d) = \frac{3}{2} P i_q [\psi_{pm} + (L_d - L_q) i_d] \tag{3}$$

where T_e is the torque, i_{dq}, and ψ_{dq} are the dq-axes components of current and flux linkage respectively, L_{dq} are the dq-axes inductances, ψ_{pm} is the permanent magnet flux linkage, and P is the number of pole pairs. According to Equation (3), the current torque component i_q and excitation component i_d follows the voltage equations, which are

$$\begin{bmatrix} u_d \\ u_q \end{bmatrix} = \begin{bmatrix} R_s & 0 \\ 0 & R_s \end{bmatrix} \cdot \begin{bmatrix} i_d \\ i_q \end{bmatrix} + \frac{\mathrm{d}}{\mathrm{d}t} \begin{bmatrix} \psi_d \\ \psi_q \end{bmatrix} + \omega_r \begin{bmatrix} 0 & -1 \\ 1 & 0 \end{bmatrix} \begin{bmatrix} \psi_d \\ \psi_q \end{bmatrix} \tag{4}$$

$$\begin{bmatrix} \psi_d \\ \psi_q \end{bmatrix} = \begin{bmatrix} L_d & 0 \\ 0 & L_q \end{bmatrix} \cdot \begin{bmatrix} i_d \\ i_q \end{bmatrix} + \begin{bmatrix} \psi_{pm} \\ 0 \end{bmatrix} \tag{5}$$

where u_d and u_q are the voltages in the dq coordinate system and R_s is the stator phase resistance. To execute the current decoupling in closed-loop control, the rotor position angle θ_r is required by the transformation from static abc-coordinate to rotary dq- coordinate. Under normal conditions, the position sensor can provide reliable speed and position angle information in the full speed range. However, in the case of sensor failure, the key information is absent but can be supplemented by the sensorless algorithm.

2) FLUX OBSERVER BASED SENSORLESS METHOD

Considering that the HF injection method is not suitable for vehicle applications, the back-EMF flux-observer-based FOC and I-F control are selected for wide speed range sensorless control when sensor failures. In the static $\alpha\beta$ coordinate system, the mathematical model of permanent magnet (PM) motor turns to be

$$\begin{cases} u_\alpha = R_s i_\alpha + \dfrac{d}{dt}(L_s i_\alpha + \psi_{pm} \cdot \cos\theta_r) \\ u_\beta = R_s i_\beta + \dfrac{d}{dt}(L_s i_\beta + \psi_{pm} \cdot \sin\theta_r) \end{cases} \tag{6}$$

According to equation (6), the estimated values of flux linkage, angle, and speed can be estimated through the flux observer as Equations (7)-(9)

$$\psi_{\alpha\beta} = HPF[\int (u_{\alpha\beta} - R_s \times i_{\alpha\beta}) \cdot dt] \tag{7}$$

$$\theta_{r\_est} = \tan^{-1} \frac{\psi_\beta - L_s i_\beta}{\psi_\alpha - L_s i_\alpha} \tag{8}$$

$$\omega_{r\_est} = \frac{d\theta_r}{dt} \tag{9}$$

where $L_s = (L_d + L_q)/2$ is the equivalent phase inductance, and the HPF is designed as a high-pass filter with low cut-off frequency to eliminate the zero drift of flux integration. The back-EMF flux estimation method uses the fundamental components in the $\alpha\beta$ static coordinate system to realize the rotor position detection, which can achieve good anti-disturbance characteristics in the high-speed range with the load. The estimation results are only affected by the stability of electrical signal samplings and the motor parameters' accuracy. However, in the low-speed range, the signal-to-noise ratio is very low due to the small amplitude of back-EMF, so the estimated results are not robust enough to make the system stable on load conditions and therefore can only be used to judge the sensor failure.

3) I-F CONTROL BASED SENSORLESS METHOD

In the low-speed range, the I-F current frequency ratio control method is adopted. Since it is impossible to obtain a stable rotor position signal by the back-EMF position estimator, an open-loop current frequency generator [20] is designed to obtain position information and perform current closed-loop control based on expected amplitude and phase angle, as shown in Fig. 2.

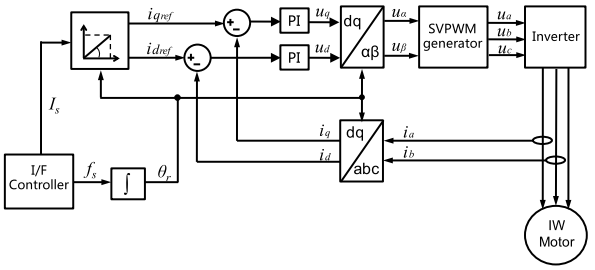

FIGURE 2. Structure diagram for I-F control system.

As shown in Fig. 3, in I-F control mode the controller gives the current vector command along with the stator d*q* coordinate system. The current establishes the rotating magnetic field and drives the permanent magnet rotor to rotate along the lagging dq coordinate. In this case, the stator current and rotor flux are not decoupled, and the output torque can be expressed as

$$T_e = \frac{3}{2} P i_q^* \cos\theta_L [\psi_{pm} + i_q^* \sin\theta_L (L_d - L_q)] \tag{10}$$

where i_q^* is the desired stator current set by the current frequency generator, and θ_L is the angle between the stator current and the rotor flux, defined as the torque angle. In the

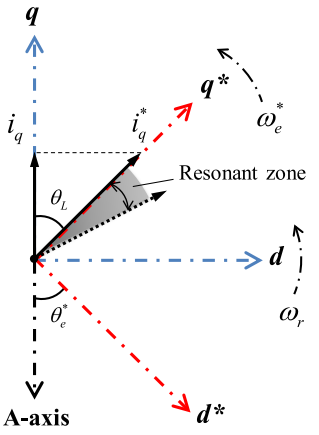

FIGURE 3. Phasor diagram of I-F control system and its oscillation process.

I-F control operation with load, the amplitude of torque angle θ_{L} reveals a slow self-stable resonance due to the balanced relationship between driving torque T_{e} and load torque T_{L}. The balance point of torque oscillation, so-called angle θ_{L0}, is between 0 and $\pi/2$. Ignoring the second term of torque equation (10), the resonance process can be expressed as a set of second-order transcendental equations

$$\begin{cases} \dfrac{d\theta_L(t)}{dt} = \omega_e^*(t) - \omega_r(t) \\ \dfrac{d\omega_r(t)}{dt} = \dfrac{1}{JP}(T_e - T_L) \\ T_e = K_T \cdot i_q^* \cdot \cos\theta_L(t) \end{cases} \tag{11}$$

where $K_T = 1.5P\psi_{\mathrm{PM}}$ is the torque constant, ω_e^* is the angular frequency of stator current output by the generator, and J is the moment of inertia of the motor. From (11), the approximate analytical solutions of torque angle and speed can be solves as

$$\theta_L(t) \approx \theta_{L0} + \cos(\sqrt{W}t) - 1 \tag{12}$$

$$\omega_r(t) = \omega_e^*(t) - \sqrt{W}\sin(\sqrt{W}t) \tag{13}$$

where the resonance factor is

$$W = \frac{K_T i_q^* \cos\theta_{L0} - T_L}{J} \geq 0 \tag{14}$$

It can be concluded that the resonance process is related to the driving torque, load torque, and moment of inertia, and the stability condition $W \geq 0$ is required. To prevent the resonant oscillation from divergence, the trigonometric function terms of (12) and (13) need to satisfy the stability condition (14), which yields

$$i_q^* \geq i_{q0}^* \tag{15}$$

where

$$i_{q0}^* = \frac{T_L}{K_T}\cos\theta_{L0} \tag{16}$$

When satisfying the stability condition, the resonance frequency is obtained

$$\omega_{IF} = \sqrt{\frac{K_T i_q^* \cos\theta_{L0} - T_L}{J}} \tag{17}$$

Fig.4 shows the resonant performance under different current settings. The system will be stable when the ratio of $i_{\mathrm{q}}^*/i_{\mathrm{q0}}^*$ is greater than 1, but be fast divergent when the ratio is less than 1. From (17) it can be concluded that the resonance frequency is positively correlated with torque current, inversely correlated with load torque, and inversely proportional to inertia. Due to the large unsprung mass and large inertia of the vehicle drive unit, the resonant frequency is normally low and smooth. Therefore, the I-F resonant state can be regarded as a quasi-steady process.

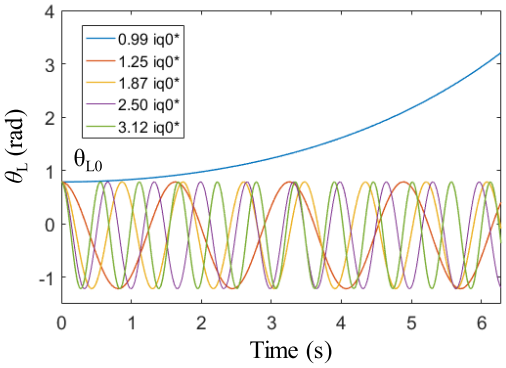

FIGURE 4. The resonant performance of torque angle concerning the desired current.

III. MULTI-STATE SWITCHING PROCESSES IN WIDE SPEED RANGE

Once the sensor failure logic is triggered, the in-wheel motor needs to decelerate from high speed running to limp or stop. During the deceleration process, the multi-state FTC strategy implements three consecutive states of sensor FOCs, sensorless FOCs, and I-F controls, as shown in Fig. 5. The specific mechanism of the strategy is designed as follows: when the position sensor is healthy, the position information needed by current vector decoupling is acquired from the sensor. At the moment of sensor failure, the controller enables the sensorless control mode, replaces the position sensor information with the sensorless algorithm information, and selects the sensorless control scheme according to the instant average speed. In the low-speed range, the I-F control is adopted to avoid the stability defect of the back-EMF algorithm, whilst in the middle and high-speed range, the back-EMF-based algorithm is applied to realize the sensorless FOC with good stability and dynamic performance.

After switching from FOC state to I-F control state, the torque and speed fluctuations may appear in a short time since the magnitude and phase of the current vector are discontinuous. To reduce the impact at the moment of switching, a gradual transition process for the current vector is proposed, as shown in Fig. 6. Under the FOC state the optimal torque current i_{q} is located along the q-axis, and after switching to I-F state the current i_{q}^* is located at the resonant equilibrium point θ_{L}. To satisfy the torque continuity, the magnitude, and phase relationship before and after current vector transition can be expressed as follows

$$\begin{cases} i_q^*(t_0 + t_n) = i_q(t_0) \cdot \cos\theta_L \\ \arg[i_q^*(t_0 + t_n)] = \arg[i_q(t_0)] - \theta_L \end{cases} \tag{18}$$

where t_0 and t_{n} represent the initial and the completion moment of the transition process. According to the resonant characteristic in the I-F state, the current frequency is kept stable and its amplitude and phase angle are changed slowly in the transition process

$$\begin{cases} \theta_e^*(t+1) = \theta_e^*(t) - \omega_e^* t \\ i_q^*(t+1) = i_q^*(t) + \Delta i_q \end{cases} \tag{19}$$

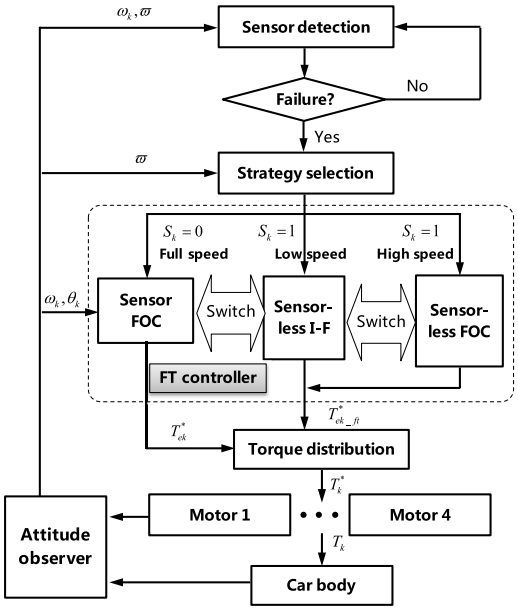

FIGURE 5. Position sensor failure determination and multi-state fault-tolerant control strategy.

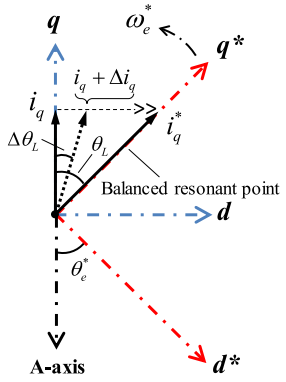

FIGURE 6. State smooth-switching process of current vectors.

where Δi_q is the current iteration step. To meet requirements of continuity, the current amplitude and phase angle are designed to converge to the balanced resonance point synchronously, and the torque angle transits smoothly from 0 degrees to θ_{L0}, so that the smoothness of torque and speed during switching is significantly improved.

IV. SIMULATION ANALYSIS AND EXPERIMENTAL VERIFICATION

The section is to verify the performance of the control strategy under simulations and experiments respectively. The simulation platform takes a 50kW in-wheel motor applied on conventional electric vehicles as the analysis object. The FTC strategies based on position sensors and sensorless algorithms are built in the Simulink, to analyze the influence of system parameters on the performance. For experiments, a 3kW in-wheel motor used in the light vehicle is taken as the test object. As shown in Fig. 7, the platform including an in-wheel

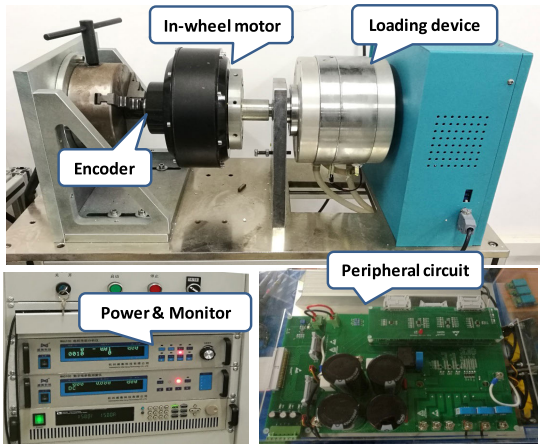

FIGURE 7. The experimental platform of in-wheel motor.

motor, an STM32F3 series controller with peripheral circuits and loading devices. An incremental photoelectric encoder is used as the position sensor. To verify the stability of the proposed FTC process under faulty conditions, the unhealthy encoder signals with electromagnetic noise can be obtained by suspending the ground terminal of the cable shield. The parameters of motor A and B are shown in Table 1.

TABLE 1. Specification of in-wheel motors.

Motor A – Standard power			
DC-bus voltage	300 V	Stator resistance	0.087 Ω
Continuous power	50 kW	Stator inductance	1.03 mH
Continuous torque	400 Nm	Pole pairs	10
Max. speed	1200 r/min	Unsprung inertia	3.0 kg·m^2
Motor B – Light power			
DC-bus voltage	72 V	Stator resistance	0.233 Ω
Continuous power	3 kW	Stator inductance	3.6 mH
Continuous torque	37 Nm	Pole pairs	23
Max. speed	1000 r/min	Body inertia	0.18 kg·m^2

A. FAILURE ANALYSIS OF POSITION SENSOR

The common faults for position sensors are pulse counting errors caused by electromagnetic interference or signal loss caused by the abnormal power supply. Fig. 8 reveals the phase A and phase B signals of the encoder being interfered with by the motor shaft current. Fig. 9 compares the measured angles between normal and disturbed conditions. It can be seen that the measured angle error accumulates with time, and finally exceeds the threshold and triggers the sensor failure logic consequently.

According to the error accumulation process, the error threshold is usually given as $\gamma = 45\,^\circ$ to prevent the motor from over-current and out-of-step. Meanwhile, the command current i_q^* is $\sqrt{2}$ times of the FOC torque current i_q and the initial value of the torque angle $\cos\theta_{L0}$ yields to $\pi/4$. Therefore, the system can switches into the sensorless FOC state or I-F state at this moment since it has a sufficient stability margin. Similarly, if the sensor encounters sudden power failure, the accumulated angle error will break through the

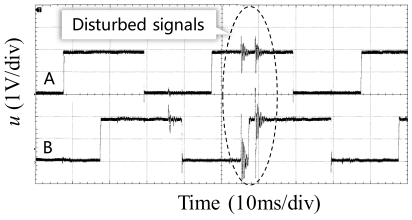

FIGURE 8. The waveform of encoder signals under interference.

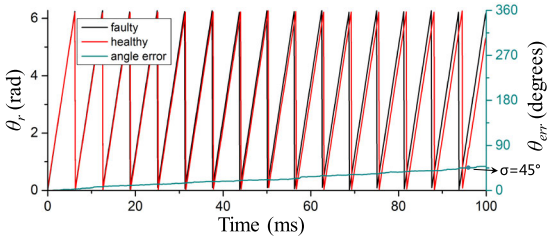

FIGURE 9. Angle comparison of position sensor before and after interference.

threshold quickly and trigger the sensorless control strategy immediately.

B. SIGNAL-NOISE ANALYSIS OF SENSORLESS ALGORITHMS

The sensorless algorithm requires accurate rotor angle information as a reference signal for sensor failure judgment. To make the trigger reliable, the inherent noise of the estimated angle by sensorless algorithm needs to be verified in advance. Fig. 10 shows the comparison of the measured and the estimated angles under steady operation with load at the speed of 600 r/min. The deviation between the measured and the estimated values is defined as noise $\Delta\theta$. Compared with the error threshold of 45 electric degrees as the true signal, the estimated error is within 2.37 electric degrees as the noise, which results in a wide tolerance for faulty judgment of the position sensor. Fig. 11 shows the variations of the $\Delta\theta$ with respect to rotating speed and time. It can be seen that the error angle gradually deviates from the reference value with the increase of the speed, and fluctuates periodically with the fundamental electric frequency. This feature is due to the mutual influence by system sampling delay and the periodic distribution of the stator inductances. Besides, it reveals that the maximum noise is no more than 4 electric degrees at rated speed, thus setting the threshold of 45 electric degrees can achieve a sufficient tolerant margin compared with the noise. To investigate the signal-to-noise tolerance, error variations with respect to electric frequency are summarized in Fig. 12, which indicates that the Signal-to-Noise Ratio (SNR) is significant in the wide speed range. Therefore, the proposed criterion for sensor failure judgment is reliable.

C. ANALYSIS OF STATE SWITCHING PROCESS

Fig. 13 shows the operating curves of the in-wheel motor A during startup and switching process from sensor FOC

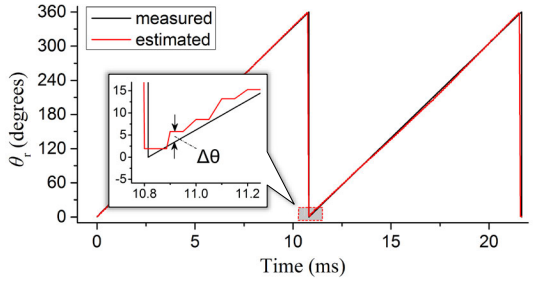

FIGURE 10. The comparison between measured and estimated positions under load at 600r/min.

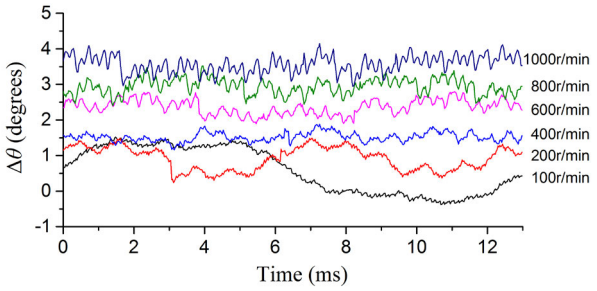

FIGURE 11. The estimated position error with respect to rotating speed and time.

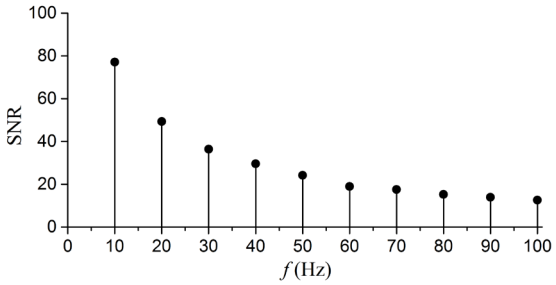

FIGURE 12. The signal-to-noise ratio of position error with respect to frequency.

to sensorless FOC at 600r/min with 200Nm heavy load. The error angle θ_{err} is defined as the deviation between the reference rotor angle θ_{r}^{*} applied in the FOC controller and the actual rotor electric angle θ_{r}. When the sensor is healthy, the applied angle is equal to the measured rotor angle, hence θ_{err} remains zero. In the faulty state, the error accumulates and grows continuously, results in torque deteriorating and speed dropping. Finally, the state switching logic is triggered when θ_{err} reaches the threshold of 45 degrees. At this moment, the position angle of the sensor is replaced by the estimated angle of the sensorless algorithm, and θ_{r}^{*} changes suddenly from 45 degrees to 0 degrees and causes slight torque fluctuation. After the switch is completed, the system recovers stability and operates at the state of sensorless FOC.

Fig. 14 shows the operating curves of motor A running at low speed and switching from sensor FOC to sensorless I-F at 100r/min and 50Nm with a light load. At the switching moment, the command current i_{q}^{*} is given as $\sqrt{2}\ i_{\mathrm{q}}$, and

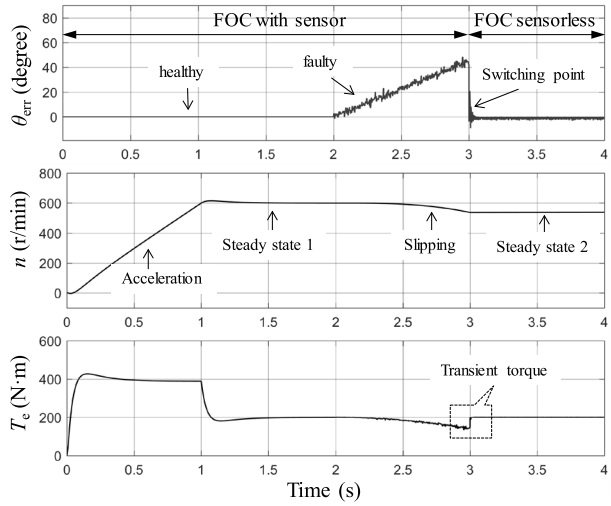

FIGURE 13. The state-switching process of FOCs from with sensor to sensorless state.

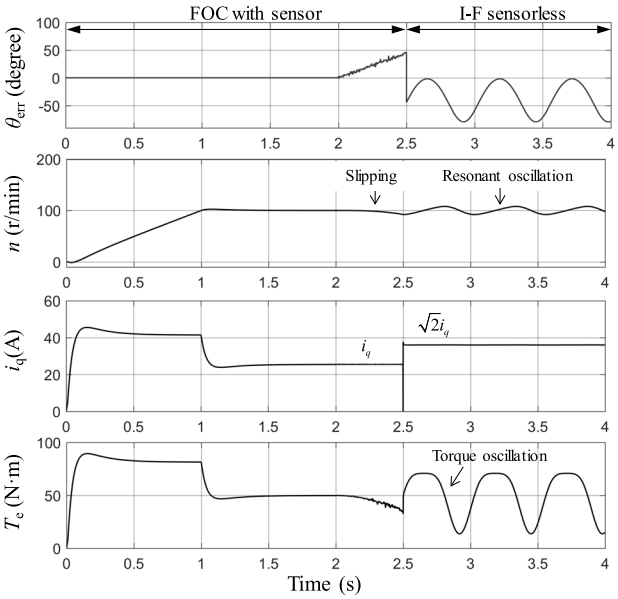

FIGURE 14. The state-switching process from FOC with sensor to sensorless I-F state.

the position angle $\theta_r^{\#}$ changes from leading 45 degrees to lagging 45 degrees, then the speed and torque appear constant oscillation in the I-F control state. According to the resonant characteristics mentioned in Equations (12) (13), the oscillation performance of different command currents is tested and shown in Fig. 15. It can be seen that if the torque component of the command current i_q^* is greater than the load torque, the system can meet the stability condition. With the increase of i_q^*, the redundant torque margin increases and the system robustness against torque impact enhances, but the oscillatory amplitudes of speed and torque increase accordingly. If further increasing i_q^*, the balanced point may approach d-axis, which results in divergent resonance gradually. This phenomenon is due to the d-axis magnetic saturation effect

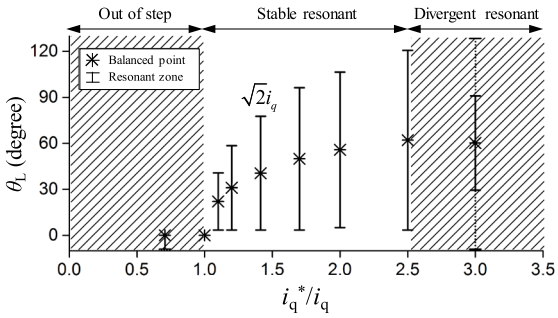

FIGURE 15. The relationship between reference current and torque angle in I-F state.

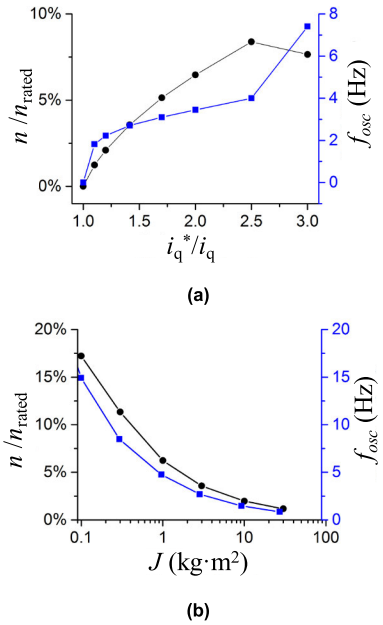

FIGURE 16. Influence of system parameters on speed fluctuation in I-F state: (a) Influence of reference current on speed fluctuation; (b) Influence of system inertia on speed fluctuation.

that makes the instant torque not equal on the positive and negative sides of the balanced point while the torque angle is oscillating. Therefore, the optimal resonant performance can be obtained by setting the balanced torque angle at 45 degrees with $\sqrt{2}i_{q0}^*$. In addition, Fig. 16 (a) and (b) show the influence of different command current and system inertia on the speed fluctuation. It can be concluded that the amplitude and frequency of speed fluctuation are positively correlated with the command current i_q^*, and inversely correlated with the inertia J. Therefore, smaller speed fluctuation and lower oscillation frequency can be obtained by selecting smaller command current and larger unsprung mass, which is prone to improve the riding performance under I-F control state.

D. SAFE DECELERATION PROCESS OF MULTI-STATES FAULT TOLERANT CONTROL

The experiments of the safe deceleration process on motor B are implemented by comparison between with FTC strategy

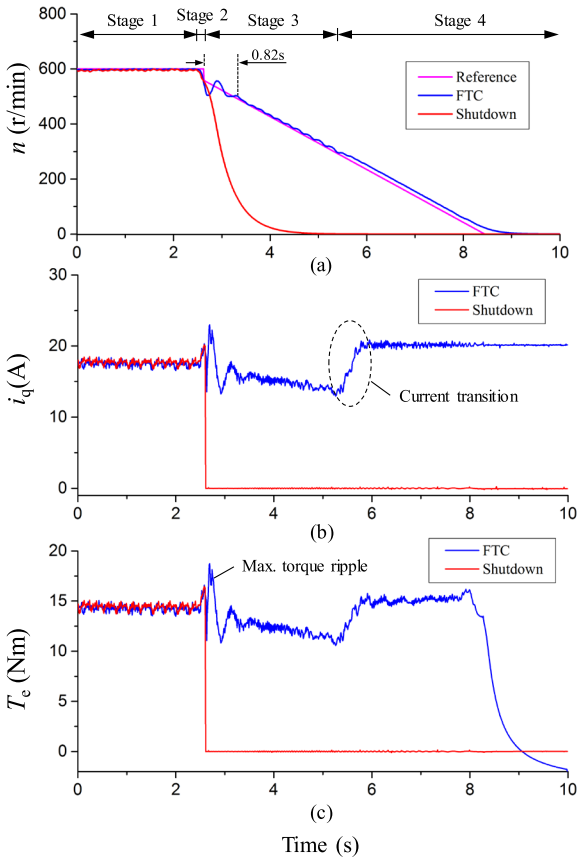

FIGURE 17. **Deceleration process with FTC strategy and with fast protective shutdown strategy.**

and with fast protective shutdown strategy, as shown in Fig.17. The process consists of 4 consecutive stages, which are the FOC steady running with healthy position sensor as stage 1, the FOC with the faulty sensor as stage 2, the FOC with the sensorless algorithm as stage 3, and the I-F control as stage 4. In Fig.17 (a), at the beginning of stage 2 when t = 2.5s, the disturbing signals of the position sensor are applied, and the position error accumulates for approximately 120ms before breaking through the 45° threshold. When the fault logic triggers, the shutdown strategy makes a sudden power cutoff for system protection, and the motor speed coasts down to zero rapidly. On the contrary, the FTC strategy replaces measured position signals with sensorless signals and keeps drive power online. As a result, the slope of speed deceleration with FTC is much smoother than that of the shutdown strategy. However, slight speed ripples can be observed in early stage 3, which are caused by the discontinuous transition of the current vector angle. The speed is stabilized by the current loop in 0.82s and then kept stable persistently. When the speed slows down to 300r/min, the gradual transition process of current is implemented. The transition interval is designed to be 400ms and the current slope rate is 10A/s. The motor cuts into the sensorless I-F stage 4 and continues to decelerate until standstill without significant speed fluctuations. As observed from the torque and current curves in Fig.17 (b) and (c), although some little fluctuations can be observed during the state-switching process, the machine can smoothly decelerate from risky high speed to a safe speed range, which verifies that the proposed strategy integrating with the transition process can achieve quick current converge and consecutive torque under sensorless conditions, so that makes the risk-controlling process stable and smooth. Besides, for the multi-wheel drive system, the torque output by other redundant drive units can compensate the torque loss on the faulty wheel, so as to further weaken the influence of sensor failure on the speed fluctuation.

V. CONCLUSION

An improved multi-states fault-tolerant control strategy for safe deceleration under the condition of position sensor failure is proposed in this paper, which utilizes the sensorless FOC and sensorless I-F methods. In the proposed strategy, a redundant verification mechanism is designed to judge the position sensor failure effectively, and a smooth transition process is implemented to guarantee the continuities of current and torque during state switching. With the switching strategy, the in-wheel motor can realize tolerant operation in the wide speed range without position sensor information. The performance of resonance stability in the I-F control state is analyzed, and the tuning principles of optimal torque angle and torque current are given. In summary, by setting the balanced torque angle at 45 degrees with a current amplitude of $\sqrt{2}i_{q0}^*$ can achieve sufficient tolerant margin and good stability in I-F runnings. Finally, the experiment shows that by controlling the slope rate of phase and amplitude of the current during deceleration, the discontinuity of multi-states switching can be solved, and the serious torque and speed fluctuation can be avoided as well. Therefore, the safety and riding comfort of electric vehicles with distributed in-wheel motor drives are greatly improved.

REFERENCES

[1] B. Guo and Y. Chen, "Robust adaptive fault-tolerant control of four-wheel independently actuated electric vehicles," *IEEE Trans. Ind. Informat.*, vol. 16, no. 5, pp. 2882–2894, May 2020, doi: 10.1109/TII.2018.2889292.

[2] Z. Yu, B. Leng, L. Xiong, Y. Feng, and F. Shi, "Direct yaw moment control for distributed drive electric vehicle handling performance improvement," *Chin. J. Mech. Eng.*, vol. 29, no. 3, pp. 486–497, May 2016, doi: 10.3901/CJME.2016.0314.031.

[3] L.-Y. Hsu and T.-L. Chen, "An optimal wheel torque distribution controller for automated vehicle trajectory following," *IEEE Trans. Veh. Technol.*, vol. 62, no. 6, pp. 2430–2440, Jul. 2013, doi: 10.1109/TVT.2013.2246593.

[4] H. Zhang, W. Zhao, and J. Wang, "Fault-tolerant control for electric vehicles with independently driven in-wheel motors considering individual driver steering characteristics," *IEEE Trans. Veh. Technol.*, vol. 68, no. 5, pp. 4527–4536, May 2019, doi: 10.1109/TVT.2019.2904698.

[5] C. Lin, S. Liang, J. Chen, and X. Gao, "A multi-objective optimal torque distribution strategy for four in-wheel-motor drive electric vehicles," *IEEE Access*, vol. 7, pp. 64627–64640, May 2019, doi: 10.1109/ACCESS.2019.2917313.

[6] Q. Wang, Y. Zhao, Y. Deng, H. Xu, H. Deng, and F. Lin, "Optimal coordinated control of ARS and DYC for four-wheel steer and in-wheel motor driven electric vehicle with unknown tire model," *IEEE Trans. Veh. Technol.*, vol. 69, no. 10, pp. 10809–10819, Oct. 2020, doi: 10.1109/TVT.2020.3012962.

[7] K. Lee and M. Lee, "Fault-tolerant stability control for independent four-wheel drive electric vehicle under actuator fault conditions," *IEEE Access*, vol. 8, pp. 91368–91378, May 2020, doi: 10.1109/ACCESS.2020.2994530.
[8] L. Zhai, T. Sun, and J. Wang, "Electronic stability control based on motor driving and braking torque distribution for a four in-wheel motor drive electric vehicle," *IEEE Trans. Veh. Technol.*, vol. 65, no. 6, pp. 4726–4739, Jun. 2016, doi: 10.1109/TVT.2016.2526663.
[9] G. Zhang, H. Zhang, X. Huang, J. Wang, H. Yu, and R. Graaf, "Active fault-tolerant control for electric vehicles with independently driven rear in-wheel motors against certain actuator faults," *IEEE Trans. Control Syst. Technol.*, vol. 24, no. 5, pp. 1557–1572, Sep. 2016, doi: 10.1109/TCST.2015.2501354.
[10] Y. Fan, R. Cui, and A. Zhang, "Torque ripple minimization for inter-turn short-circuit fault based on open-winding five phase FTFSCW-IPM motor for electric vehicle application," *IEEE Trans. Veh. Technol.*, vol. 69, no. 1, pp. 282–292, Jan. 2020, doi: 10.1109/TVT.2019.2953689.
[11] Y. Fan, W. Zhu, X. Zhang, M. Cheng, and K. T. Chau, "Research on a single phase-loss fault-tolerant control strategy for a new flux-modulated permanent-magnet compact in-wheel motor," *IEEE Trans. Energy Convers.*, vol. 31, no. 2, pp. 658–666, Jun. 2016, doi: 10.1109/TEC.2015.2498613.
[12] S. Kwak, T. Kim, and G. Park, "Phase-redundant-based reliable direct AC/AC converter drive for series hybrid off-highway heavy electric vehicles," *IEEE Trans. Veh. Technol.*, vol. 59, no. 6, pp. 2674–2688, Jul. 2010, doi: 10.1109/TVT.2010.2050792.
[13] Y. Chen, G. Götting, L. Chen, and J. Xie, "A design of stabilized sensor-error-tolerant V/f control in iPMSMs for EV traction," in *Proc. 27th Int. Workshop Electr. Drives, MPEI Dept. Electr. Drives 90th Anniversary (IWED)*, Moscow, Russia, Jan. 2020, pp. 1–8, doi: 10.1109/IWED48848.2020.9069573.
[14] N. Jeon and H. Lee, "Integrated fault diagnosis algorithm for motor sensors of in-wheel independent drive electric vehicles," *Sensors*, vol. 16, no. 12, p. 2106, Dec. 2016, doi: 10.3390/s16122106.
[15] Y. Li, H. Wu, X. Xu, X. Sun, and J. Zhao, "Rotor position estimation approaches for sensorless control of permanent magnet traction motor in electric vehicles: A review," *World Electr. Vehicle J.*, vol. 12, no. 1, p. 9, Jan. 2021, doi: 10.3390/wevj12010009.
[16] T. Wu, D. Luo, S. Huang, X. Wu, K. Liu, K. Lu, and X. Peng, "A fast estimation of initial rotor position for low-speed free-running IPMSM," *IEEE Trans. Power Electron.*, vol. 35, no. 7, pp. 7664–7673, Jul. 2020, doi: 10.1109/TPEL.2019.2958101.
[17] G. Feng, C. Lai, K. L. V. Iyer, and N. C. Kar, "Improved high-frequency voltage injection based permanent magnet temperature estimation for PMSM condition monitoring for EV applications," *IEEE Trans. Veh. Technol.*, vol. 67, no. 1, pp. 216–225, Jan. 2018, doi: 10.1109/TVT.2017.2778429.
[18] S. Du, Li. Quan, X. Zhu, L. Zhang, and Y. Zuo, "Fault-tolerant control of position sensor failure for PMSM at zero and low speed based on high frequency injection," *Proc. CSEE*, vol. 39, no. 10, pp. 3038–3046, May 2019, doi: 10.13334/j.0258-8013.pcsee.181797.
[19] G.-D. Andreescu, C. I. Pitic, F. Blaabjerg, and I. Boldea, "Combined flux observer with signal injection enhancement for wide speed range sensorless direct torque control of IPMSM drives," *IEEE Trans. Energy Convers.*, vol. 23, no. 2, pp. 393–402, Jun. 2008, doi: 10.1109/TEC.2007.914386.
[20] J. Xing, Z. Qin, C. Lin, and X. Jiang, "Research on startup process for sensorless control of PMSMs based on I-F method combined with an adaptive compensator," *IEEE Access*, vol. 8, pp. 70812–70821, Apr. 2020, doi: 10.1109/ACCESS.2020.2987343.

ZIHUI WANG received the B.S. and Ph.D. degrees in electrical engineering from Zhejiang University, Hangzhou, China, in 2007 and 2012, respectively.

From 2009 to 2011, he was a Research Assistant with Aalborg University, Aalborg, Denmark. In 2012, he worked at the Research Center of Philips Company Ltd., Shanghai, China, as a Researcher. In 2013, he became a Lecture with the Department of Automation and Engineering, Zhejiang University of Science and Technology, Hangzhou. From 2016 to 2019, he was a Postdoctoral Researcher with Zhejiang University. His research interests include control of power electronic systems and control of permanent magnet synchronous machines with sensorless algorithms.

JINCAI SHAO received the B.S. degree from the College of Science and Technology, Ningbo University, Ningbo, China, in 2018. He is currently pursuing the M.S. degree in automobile engineering with the Zhejiang University of Science and Technology, Hangzhou, China.

His research interests include vehicle electrical appliances and automatic control and electric drive control technology.

ZHIYUAN HE received the B.S. and M.S. degrees in electrical engineering from Zhejiang University, Hangzhou, China, in 1983 and 2000, respectively.

From 1996 to 1997, he was a Research Assistant with the Technical University of Munich, Germany. From 2003 to 2004, he was a Visiting Scholar with the Institute of Power Electronics, Technical University of Berlin, Germany. Since 2007, he has been a Professor with the School of Automation and Electrical Engineering, Zhejiang University of Science and Technology, Hangzhou. His research interests include electrical engineering and power electronics. He has been the Vice President of the Zhejiang Provincial Power Supply Society, China, since 2009.